Supporting Information

Electrochemically Grown Fe_2O_3/Fe_3O_4 Heterostructure Nanotubes with In_2O_3 induced Tandem Internal Electric Fields for Enhanced Photoelectrochemical Water Oxidation

Xiaohui Yan[a], Gang Li[a,c*], Kai Shen[a], Congwei Wang[b*], Kaiying Wang [a, d*]

a Institute of Energy Innovation, Taiyuan University of Technology, Taiyuan 030024, China.

b CAS Key Laboratory of Carbon Materials, Institute of Coal Chemistry, Chinese Academy of Sciences, Taiyuan 030001, China.

c College of Physics and Information Engineering, Minnan Normal University, Zhangzhou 361000，China.

d Department of Microsystems, University of South-Eastern Norway, Horten, 3184, Norway.

*Corresponding Author, E-mail: ligang02@tyut.edu.cn, wangcongwei@sxicc.ac.cn, kaiying.wang@usn.no

Experimental Section

Preparation of the in-situ growth dual-phase iron oxide nanotubes (NTs) heterojunction

The dual-phase iron oxide NTs photoanode was prepared by an anodization method with stainless steel (SSt) foil in a two-electrode electrochemical cell. Typically, all electrochemical anodization processes were performed at room temperature of 25°C as controlled through a low-temperature thermostat bath. Commercial 50 μm-thick 304 stainless steel foil (20 mm ×10 mm) was employed as the working electrode, while a rectangular piece of graphite of 2 cm^2 was used as the counter electrode. All SSt foils were washed with acetone and ethanol in an ultrasonic cleaner for 30 min to remove oil layer, then cleaned with distilled water, and dried at 60°C for 1 h before anodization. The potentiostatic voltage of 60 V was applied for 1 h using Keithley 2400 Source Meter DC power. The ethylene glycol containing 0.1 M NH_4F and 0.1 M H_2O was used as electrolyte. The morphology and structure of anodized dual-phase iron oxide (ASSt) NTs was regulated via controlling the anodization time and applied voltages (Figure S2, Supporting Information). The electrochemically anodized samples were further calcined in Ar/H_2 (ratio of 95:5) atmosphere at 600°C for 1 h with a heating ramp of 3°C/min to prepare annealed T-ASSt photoanode. Pure Fe_2O_3 and Fe_3O_4 were fabricated by annealing the as-anodized ASSt at 600°C for 1 h in O_2 and 4 h in N_2, respectively.

Preparation of the dual-phase iron oxide NTs loaded with indium oxide (T-In@ASSt):

In_2O_3 NPs was in-situ thermally deposited onto the nanowalls of the as-anodized ASSt NTs. Briefly, a piece of prepared ASSt NTs foil was immersed in 0.1 M of indium trichloride ethanol solution, transferred to a Teflon-lined autoclave (20mL), and kept at 80 °C for 1h. The obtained foil was washed with ethanol and distilled water to remove the surface residues and subsequently calcinated at 600 °C under Ar/H_2 (ratio of 95:5) atmosphere for 1 h to obtain T-In@ASSt NTs films. Commercial Fe_2O_3 powders (Sigma-Aldrich, F108317) were also loaded on the ITO via spin-coating method as controlling sample. Pure In_2O_3 was fabricated by calcining the solution with 1.2 g indium trichloride, 15 ml DMF and 2.4 g PVP.

Material characterizations

Scanning electron microscope (SEM) images were performed on Gemini-300 executed at 5 kV. Transmission electron microscopy (TEM) images and selected area electron diffraction (SAED) were operated on JEM-2100F with accelerating voltage of 200 kV. The X-ray diffraction (XRD) was measured via an X-ray diffractometer (Empyrean-2, PANalytical B.V.) with Cu K α source under 45 kV and 40 mA. X-ray photoelectron spectroscopy (XPS) tests were performed through an AXIS Ultra DLD spectrometer with Al Kα source (hν=1486.6 eV). Raman spectroscopy tests were performed on laser Raman spectrometer

(Renishaw in Via Reflex), which possessed exciting laser light wavelength of 532 nm. Kelvin probe force microscope (KPFM) was performed on Bruker Dimension Icon with scanned area of 200 nm × 200 nm.

PEC measurements

All photoelectrochemical tests were conducted with a Zahner PP211 electrochemical workstation. The PEC experiments were performed in a three-electrode configuration system, in which the dual-phase iron oxide NTs-based film photoanodes were regarded as the working electrode, Hg/HgO (1 M KOH) electrode and Pt wire were employed as reference and counter electrodes, respectively. 1 M KOH aqueous solution was selected as electrolyte (pH ~13.6). The active area of photoanodes submerged in the electrolyte was 1.0 cm². The light source was a xenon light equipment with AM 1.5 filter. The illuminated area was 1 cm². Linear-sweep voltammograms (LSV) plots of the film photoanode were obtained via scanning potential of positive direction in a voltage range from 0.6 to 1.6 V versus RHE with a scan rate of 1 mV s^{-1} under dark and single/double illumination conditions. The electrochemical impedance spectroscopy (EIS) measurements were conducted on a frequency scale from 10M Hz to 100K Hz with 10 mV amplitude under dark and single/double illumination conditions. Mott-Schottky plots were tested from 0.2 to 1.8 V versus RHE at a frequency of 1k Hz under the dark environment. Steady-state photocurrent without applied bias potential were collected at a light source with AM 1.5 filter which was switched manually at regular 20 seconds intervals under single and double illumination conditions. The stability evaluation was performed by measuring the current density-time curve at 1.55 V_{RHE} under double-illumination condition. All potentials tested versus Hg/HgO were calibrated to the RHE through the following Equation:

$$E_{RHE} = E_{Hg/HgO} + E_{Hg/HgO}^0 + 0.059 \times PH \tag{S1}$$

in which E_{RHE} is calibrated potential versus RHE. $E_{Hg/HgO}$ represents test result versus Hg/HgO and $E_{Hg/HgO}^0$ is 0.098 V at 25 °C ambient temperature.

Applied bias photon-to-current efficiency (ABPE) was calculated via the obtained current density, employing the Equation:

$$\text{ABPE (\%)} = \frac{J \times (1.23 - V)}{P} \times 100$$

(S2)

where J is the photocurrent density (mA cm^{-2}), which could be measured via electrochemical workstation. V refers to applied bias as well as P represents incident light intensity.

Incident photon-to-current efficiency (IPCE) data were collected via a xenon light equipment with various monochromatic filters (350, 365, 380, 400, 420, 475, 550, 600, 700 nm) together with power meter of PM 100D, which was calculated by the Equation:

$$IPCE\ (\%) = \frac{1240\ J(\lambda)}{P(\lambda)\lambda} \times 100 \tag{S3}$$

where the $J(\lambda)$ represents photocurrent density (mA cm^{-2}), $P(\lambda)$ is power density of monochromatic filters (mW cm^{-2}) and the λ is referred to wavelength of light (nm).

**Atomic models and DFT computational method**

Model construction

Device Studio program was employed to perform the visualization, modeling and calculation (DS-PAW).[1] A (2×2) supercell of four-layer α-Fe$_2$O$_3$ (110) surface slab model was constructed based on the TEM observation, within which the bottom two Fe$_2$O$_3$ layers were fixed. A thickness of 20 Å vacuum was placed in the direction perpendicular to Fe$_2$O$_3$ (110) surface, so the interactions between any adjusting molecules can be safely ignored. After the structural optimization of Fe$_2$O$_3$ (110) slab, an In$_2$O$_3$ (222) cluster with 6 In atoms and 9 O atoms was modeled and integrated on top of Fe$_2$O$_3$ (110) surface.

Calculation method

All DFT computations were carried out by employing the spin-polarized plane-wave-based method and periodic slab model. The electron exchange and correlation energy were used within the generalized gradient approximation (GGA). Projected augmented wave (PAW) potential is employed to describe the electron-ion interaction and a kinetic energy cutoff of 500 eV is selected for the plane wave expansion. In order to consider more precisely the effect of the on-site Coulomb repulsion of Fe $3d$ electrons, the exchange-correlation energy is treated by the DFT + U approach (U - J = 4.3 eV). For structural optimization, the convergence criterion of total energy was set to 1×10^{-5} eV, and the atoms were relaxed until the force acting on each atom was less than 0.03 eV Å^{-1}. Brillouin-zone was sampled with $2 \times 3 \times 1$ Monkhosrt−Pack grid for slab model calculations.

The adsorption model was based on a series of aforementioned surface slab models with different adsorbates representing intermediate reactions. The Gibbs free energy (ΔG) was calculated by correcting the DFT energy with zero-point energy and entropy via $\Delta G = \Delta E + \Delta ZPE - T\Delta S$, where E is the DFT total energy, ZPE is the zero-point energy, T is the environment temperature, and S is the entropy. For ZPE correction and entropy calculation, the vibrational frequencies were calculated by applying density

functional perturbation theory. The following intermediate reactions was employed for free energy calculations, as previously suggested.

$$* + OH^- \rightarrow OH^*$$

$$OH^* + OH^- \rightarrow O^* + H_2O$$

$$O^* + OH^- \rightarrow HOO^* + e^-$$

$$HOO^* + OH^- \rightarrow * + O_2 + H_2O$$
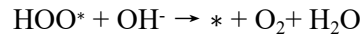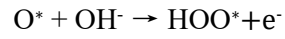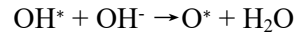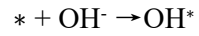
The * denotes the active sites at the catalyst surface. In order to evaluate the impact of applied bias on the OER thermodynamics, additional factor of $1eV \times E_{bias}$ was added to the above calculated free energy.
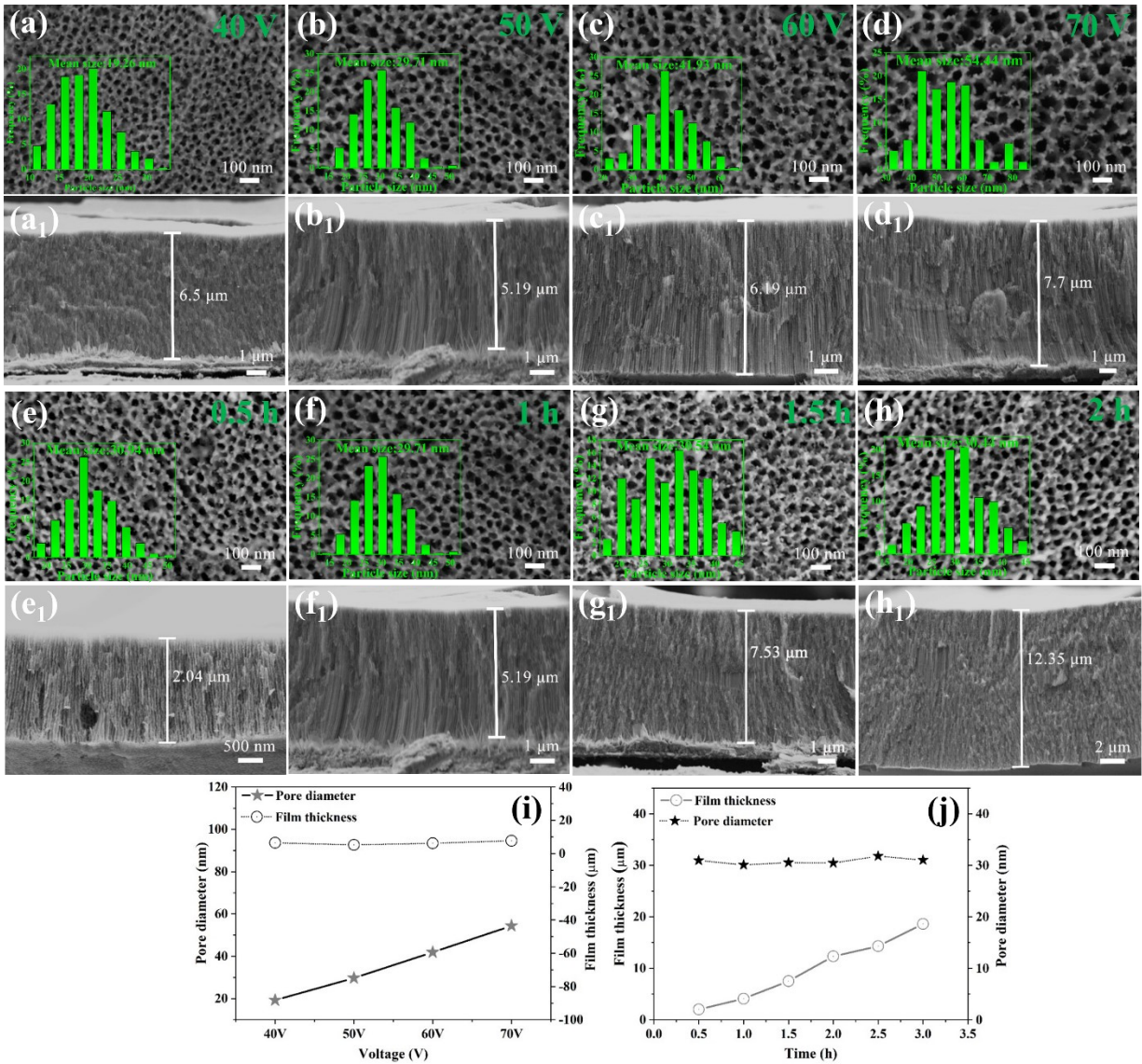
Fig. S1 (a-d) different anodized voltages (anodized time: 1 h). (e-h) different anodized time (anodized voltage: 50 V). statistical graph: (i) different anodized voltages and (j) different anodized time.
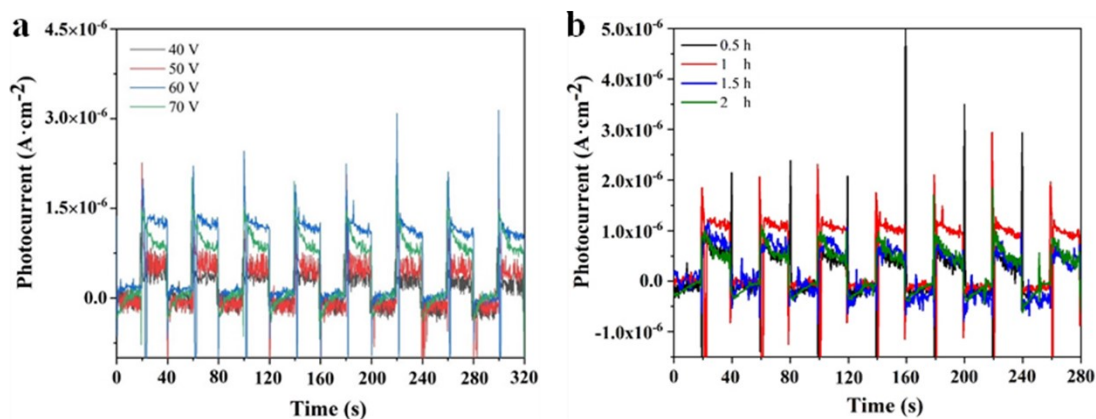
Fig. S2 Photocurrent of (a) different anodized voltages (anodized time: 1 h) and (b) different anodized time (anodized voltage: 50 V).

Based on the reported anodization method,[2] the formed nanotubular morphology was varied with different electrochemical parameters (voltage, time, etc.). Therefore, investigations on the relationship between electrochemical parameters, specifically, anodization potential and time, with the corresponding T-ASSt NTs microstructures were conducted, as shown in Fig. S1. The corresponding photo-responses of formed ASSt NTs was evaluated via measuring the photogenerated photocurrent (densities), as shown in Fig. S2. The 60 V, 1h electrochemical parameter was employed for the following preparation of composite photoanodes.
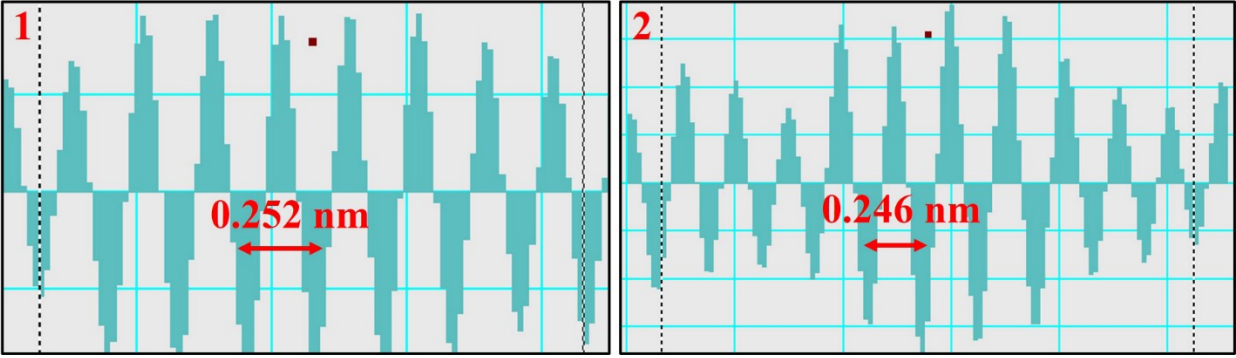
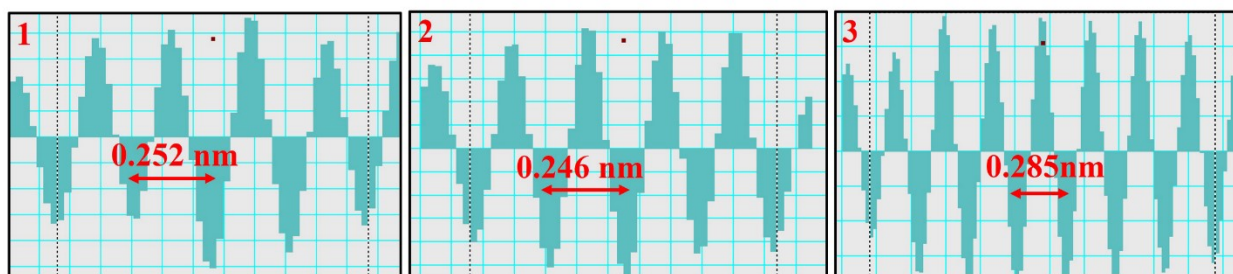**Fig. S3** Lattice fringe spacings of T-ASSt in red rectangle 1 and 2 in Fig.1g.

Fig. S4 Lattice fringe spacings of T-In@ASSt in red rectangle 1,2 and 3 in Fig.1m.
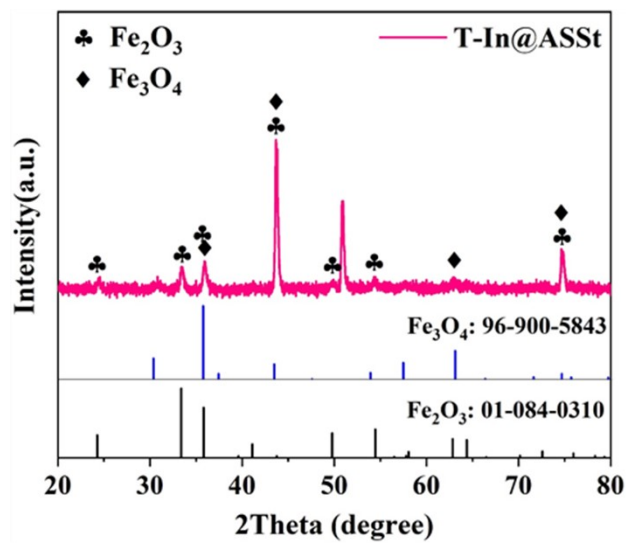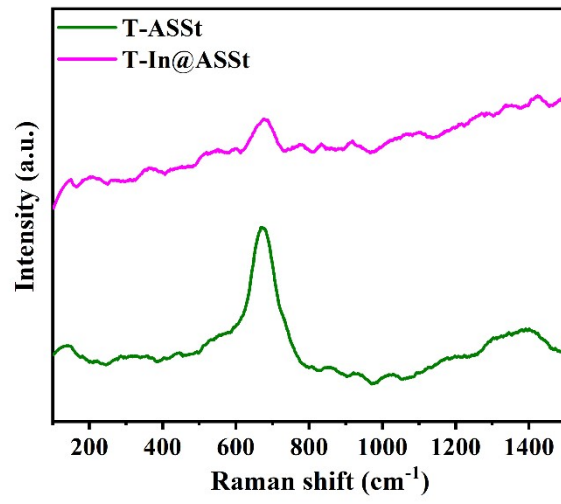
Fig. S5 XRD spectra of T-In@ASSt.

Fig. S6 The Raman spectra in the 100-3200 cm-1 region for T-ASSt and T-In@ASSt photoanodes.
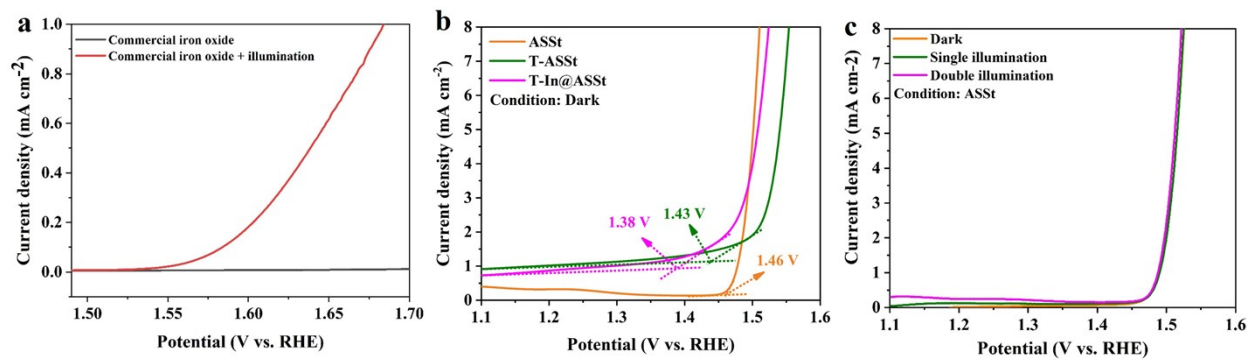
Fig. S7 The LSV curves of (a) commercial iron oxide under dark and single illumination. (b) ASSt, T-ASSt, T-In@ASSt under dark condition. (c) ASSt under dark, single and double illumination conditions.
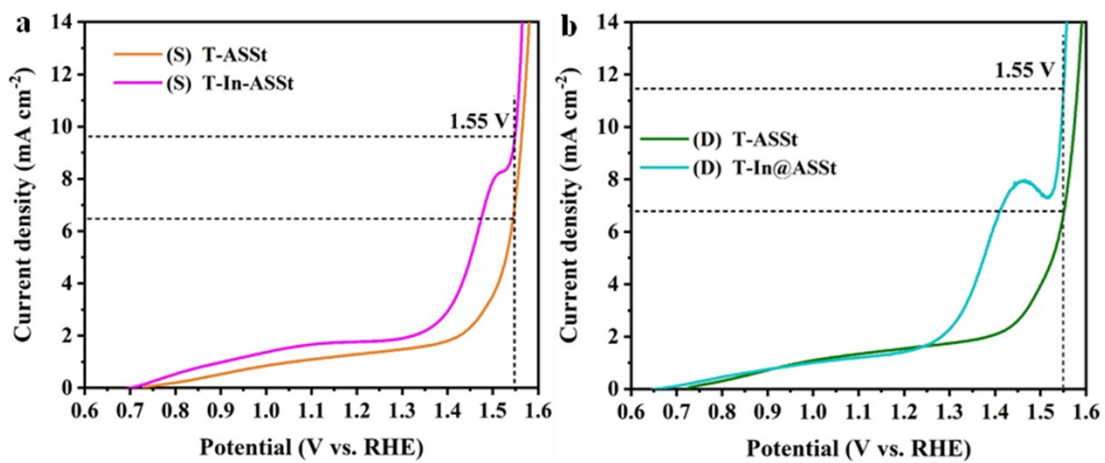
Fig. S8 The *J-V* curves of T-ASSt and T-In@ASSt photoanodes from 0.6 to 1.6 V: (a) single. (b) double illumination. (Note: S and D represent single and double illumination, respectively).
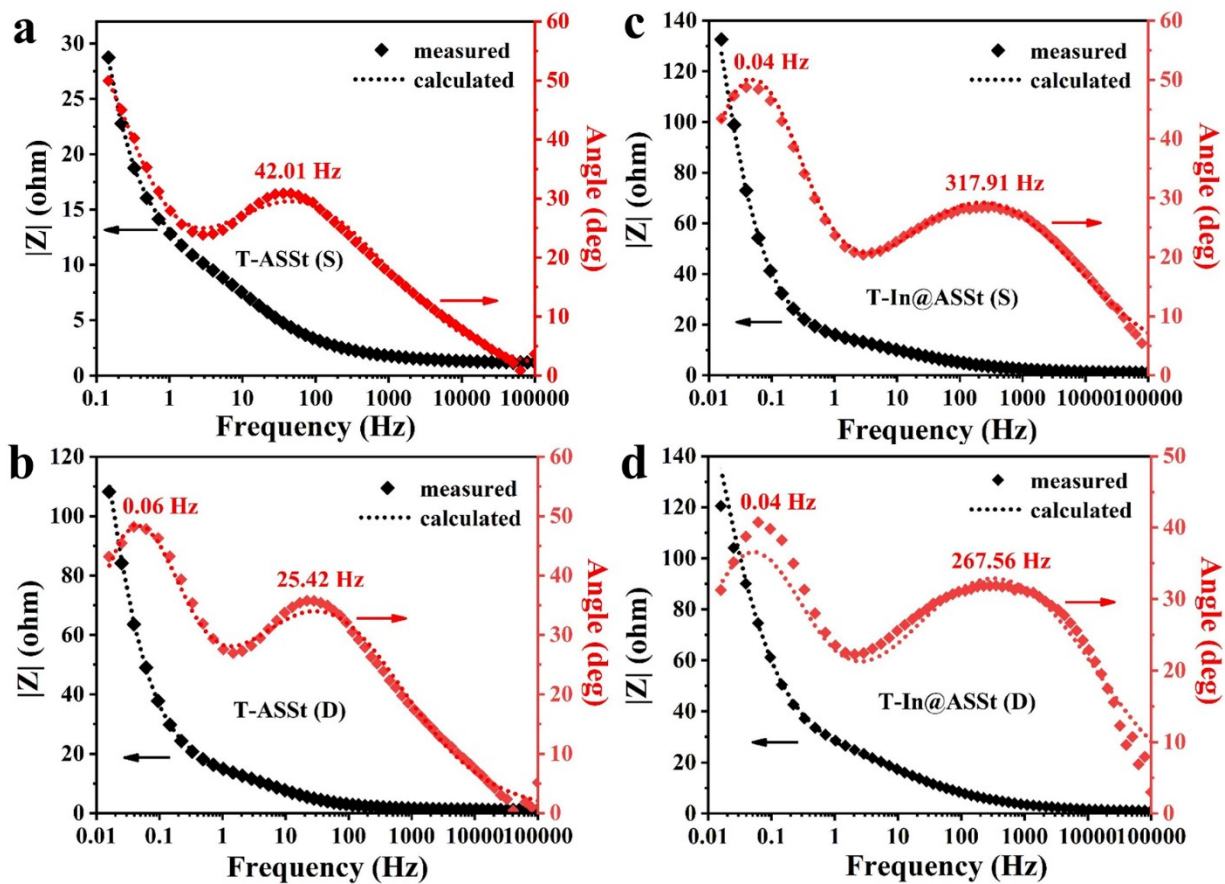
Fig. S9 Bode plots of impedance modulus spectra (left axis) superimposed with the Bode phase plots (right axis): (a) single- and (b) double-illuminated T-ASSt. (c) single- and (d) double-illuminated T-In@ASSt.
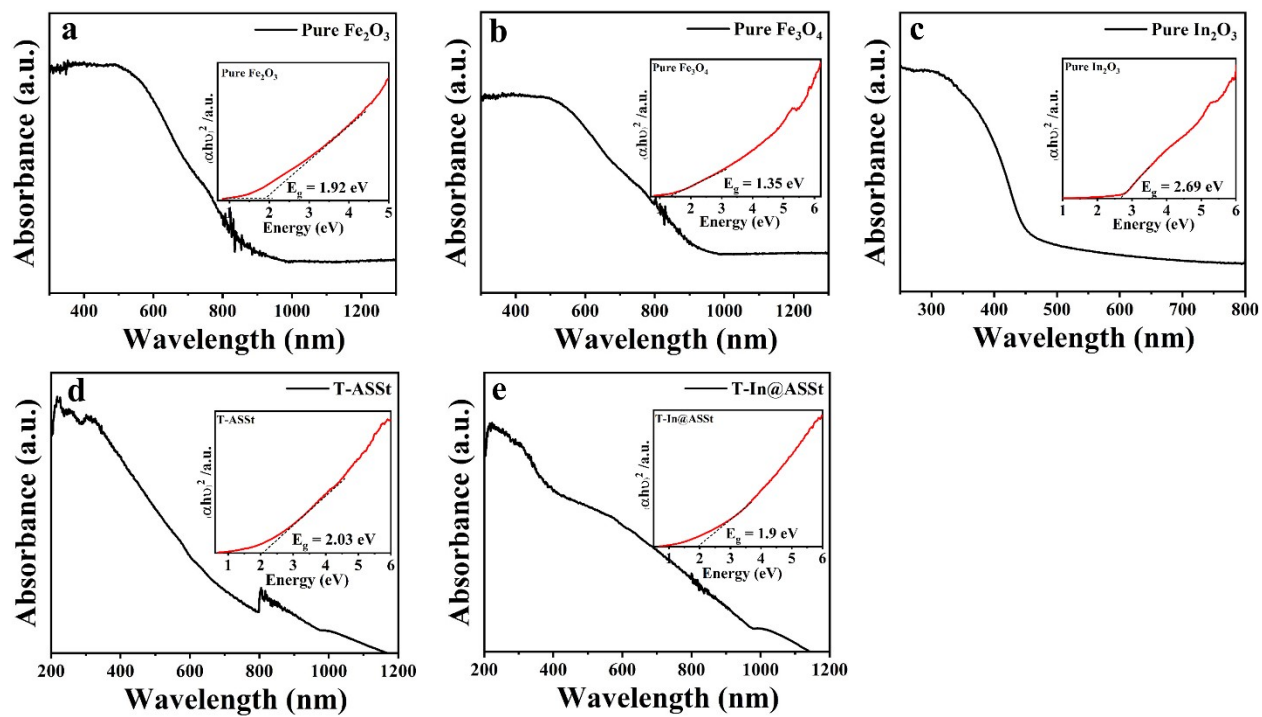
Fig. S10 UV-visible diffuse reflectance spectra of (a) pure Fe_2O_3. (b) pure Fe_3O_4. (c) pure In_2O_3. (d) T-ASSt and (e) T-In@ASSt photoanodes, the inset: Tauc's plots.

Fig. S11 Current density-time curve of the T-In@ASSt photoanode measured at 1.55 V vs. RHE under double illumination.
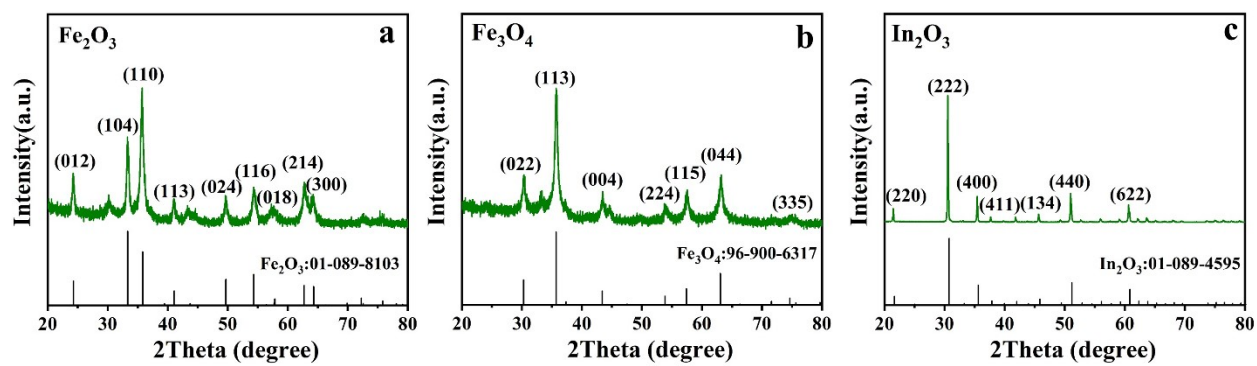
Fig. S12 The XRD spectra of (a) pure Fe_2O_3. (b) pure Fe_3O_4. (c) pure In_2O_3.
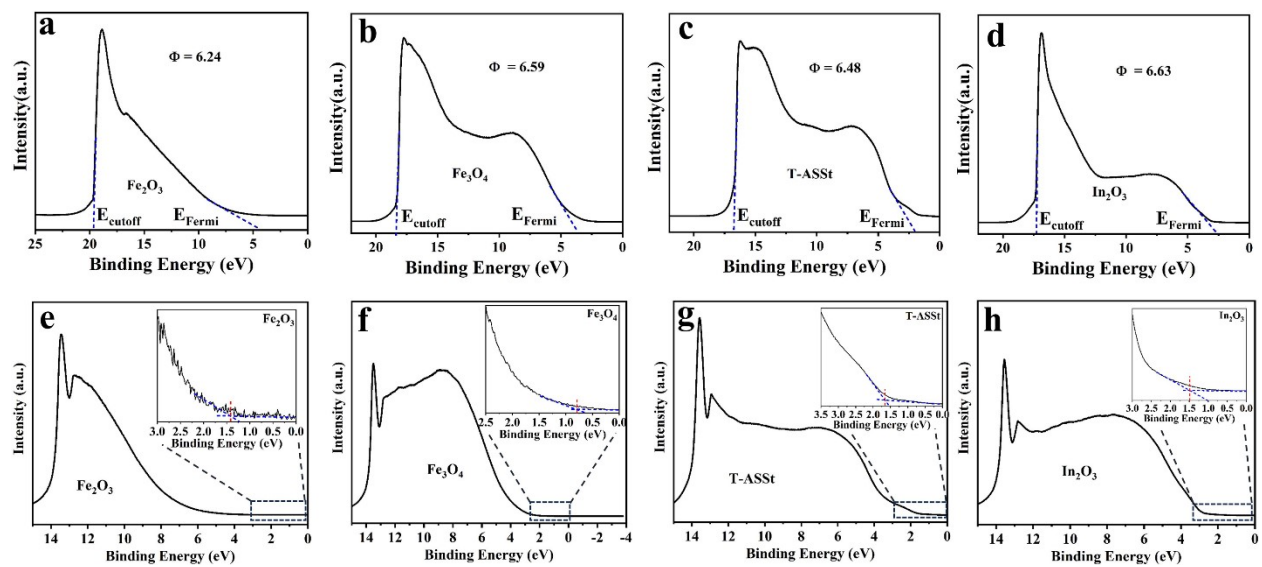
Fig. S13 UPS spectra of (a) pure Fe_2O_3. (b) Fe_3O_4. (c) T-ASSt and (d) In_2O_3 photoanodes. VB spectra of (e) pure Fe_2O_3. (f) Fe_3O_4. (g) T-ASSt and (h) In_2O_3 photoanodes.

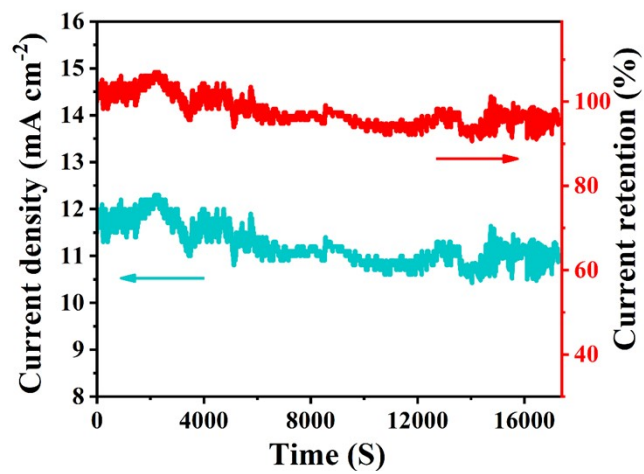**Table S1.** Parameters and reliability factors obtained by Rietveld refinements of T-ASSt and T-In@ASSt sample.

	T-ASSt		T-In@ASSt	
Phase	magnetite	hematite	magnetite	hematite
Weight fraction (%)	75.2	24.8	58.8	41.2
Lattice parameters (Å)	a: 8.39	a: 5.11 c: 12.99	a: 8.38	a: 5.03 c: 13.62
Reliability factors		Rp: 11.76 Rexp: 9.86 Rwp: 13.89		Rp: 2.39 Rexp: 2.03 Rwp: 5.51

Table S2. Comparison of EIS resistances of homojunction iron oxide-based films under different illumination conditions.

Condition	Sample	R_1 (Ω)	R_2 (Ω)	R_3 (Ω)
Single-illumination	T-ASSt	1.2	12.2	308.9
	T-In@ASSt	0.8	16.2	263.0
Double-illumination	T-ASSt	1.0	16.0	233.0
	T-In@ASSt	0.8	28.1	204.5

Table S3. Flat band potential, carrier density and depletion layer of homojunction iron oxide-based films.

Sample	V_{fb} (V)	N_d (cm^{-3})	W (nm)
ASSt	0.24	7.53×10^{18}	142.9
T-ASSt	0.27	1.16×10^{21}	11.3
T-In@ASSt	0.37	1.33×10^{21}	10.1

Table S4. Comparison of photoelectrocatalytic performances for the various iron oxide related photoanode materials in the water oxidation system.

Sample	Onset potential	ABPE	Nd (cm^{-3})	O$_2$ evolution	Ref.
Ti-Fe$_2$O$_3$ MCs	0.76 V vs. RHE	unknown	5.1×10^{20}	0.92 µmol cm^{-2} h^{-1}	3
Fe$_2$O$_3$ (Ti) MC_T	0.8 V vs. RHE	unknown	4.1×10^{21}	unknown	4
Anodized Fe foams	0.79 V vs. RHE	unknown	unknown	11 µmol cm^{-2} h^{-1}	5
Co-Pi/Co$_3$O$_4$/Ti:Fe$_2$O$_3$	0.64 V vs. RHE	0.43 %	2.83×10^{20}	unknown	6
Co-Mn-α-Fe$_2$O$_3$	~ 0.7 V vs. RHE	0.25 %	5.41×10^{20}	unknown	7
Fe$_2$O$_3$-FeO$_x$	0.8 V vs. RHE	unknown	unknown	~4.23 µmol cm^{-2} h^{-1}	8
Fe$_2$O$_3$	0.7 V vs. Ag/AgCl	unknown	5.3×10^{18}	~0.18 mmol L^{-2} h^{-1}	9
Co-Pi/MNs/α-Fe$_2$O$_3$	0.57 V vs. RHE	0.33 %	unknown	~19.5 µmol cm^{-2} h^{-1}	10
W-α-Fe$_2$O$_3$	0.85 V vs. RHE	0.22 %	1.0×10^{18}	~10 µmol cm^{-2} h^{-1}	11
In$_2$S$_3$/F-Fe$_2$O$_3$	~ 0.9 V vs. RHE	0.15 %	8.87×10^{18}	~5.57 µmol cm^{-2} h^{-1}	12
Fe$_2$O$_3$@ZIF-67	~ 0.85 V vs. RHE	0.07 %	unknown	~5.5 µmol cm^{-2} h^{-1}	13
Li@α-Fe$_2$O$_3$	0.6 V vs. RHE	0.07 %	3.33×10^{20}	unknown	14
P-Fe$_2$O$_3$/Ce-Pi	~ 0.9 V vs. RHE	unknown	7.80×10^{17}	11.6 µmol cm^{-2} h^{-1}	15
T-In@ASSt	**0.64 V vs. RHE**	**0.44%**	**1.33×10^{21}**	**71.6 µmol cm^{-2} h^{-1}**	**This work**

Supporting references

1 P. E. Blöchl, *Phys. Rev. B*, 1994, **50**, 17953-17979.

2 Y. G. Wang, G. Li, K. Y. Wang, X. Y. Chen, *Appl. Surf. Sci.*, 2020, **505**, 144497.

3 Z. J. Zhang, I. Karimata, H. Nagashima, S. Muto, K. Ohara, K. Sugimoto, *Nat. Commun.*, 2019, **10**, 4832.

4 Z. J. Zhang, H. Nagashima, T. Tachikawa, *Angew. Chem. Int. Ed.*, 2020, **59**, 9047-9054.

5 J. S. Kang, Y. Noh, J. Kim, H. Choi, *Angew. Chem. Int. Ed.*, 2017, **56**, 6583-6588.

6 S. S. Yi, B. R. Wulan, J. M. Yan, Q. Jiang, *Adv. Funct. Mater.*, 2019, **29**, 1801902.

7 G. L. Yang, Y. X. Li, H. Pang, K. Chang, J. H. Ye, *Adv. Funct. Mater.*, 2019, **29**, 1904622.

8 D. Walsh, J. F. Zhang, M. Regue, R. Dassanayake, S. Eslava, *ACS Appl. Energy Mater.*, 2019, **2**, 2043-2052.

9 B. Klahr, S. Gimenez, O. Zandi, F. Fabregat-Santiago, T. Hamann, *ACS Appl. Mater. Interfaces*, 2015, **7**, 7653-7660.

10 G. L. Yang, S. J. Li, X. S. Wang, B. Ding, Y. X. Li, H. W. Lin, D. M. Tang, X. H. Ren, Q. Wang, S. Q. Luo, J. H. Ye, *Appl. Catal. B: Environ.*, 2021, **297**, 120268.

11 T. Katsuki, Z. N. Zahran, K. Tanaka, T. Eo, E. A. Mohamed, Y. Tsubonouchi, M. R. Berber, M. Yagi, *ACS Appl. Mater. Interfaces*, 2021, **13**, 39282-39290.

12 H. Chai, L. L. Gao, P. Wang, F. Li, G. W. Hu, J. Jin, *Appl. Catal. B: Environ.*, 2022, **305**, 121011.

13 W. Z. Li, K. K. Wang, X. T. Yang, F. Q. Zhan, Y. Q. Wang, M. Liu, X. Q. Qiu, J. Li, J. Zhan, Q. H. Li, Y. Liu, *Chem. Eng. J.*, 2020, **379**, 122256.

14 J. J. Cai, L. C. Xu, X. X. Tang, L. N. Kong, J. M. Wang, R. F. Wang, X. L. Li, Q. Xie, K. K. Mao, H. J. Pan, *J. Alloy. Compd.*, 2022, **915**, 165349.

15 X. B. Bu, Y. X. Gao, S. H. Zhang, Y. Tian, *Chem. Eng. J.*, 2019, **355**, 910-919.